

# Dual-Color Emission from Monolithic *m*-Plane Core–Shell InGaN/GaN Quantum Wells

Akanksha Kapoor, Vincent Grenier, Eric Robin, Catherine Bougerol, Gwénoél Jacopin, Bruno Gayral, Maria Tchernycheva, Joël Eymery, and Christophe Durand\*

A dual-color emission is achieved combining two monolithic sets of core–shell multiple quantum wells (MQWs) grown on GaN microwires. The shell heterostructure is composed of 3 × blue MQWs and 7 × green MQWs with photoluminescence emission covering 400–450 and 450–550 nm wavelength bands, respectively. Both emissions are coming from the two MQW sets grown on *m*-plane sidewall surface, as revealed by cathodoluminescence mapping. Advanced structural characterization combining transmission electron microscopy and energy-dispersive X-ray analysis is performed on longitudinal cross-sectional slices of the wires. Considering asymmetrical QW interface, the In content is measured to be equal to 15.7 (±0.5)% and 23.5 (±2.0)% in the first and the second MQW set consistent with the blue and green emissions. Extended defects are formed originating from the second MQW set due to higher In content. A flexible light-emitting diode (LED) is fabricated based on these dual core–shell MQWs, showing an electroluminescence dominated by green emission due to efficient hole injection in the In-rich second MQW set. This work opens the way for multiple color emission from core–shell MQWs for phosphor-free nanowire-based LED applications.

## 1. Introduction

The current technology for white light-emitting diodes (LEDs) is based on a blue electroluminescence (EL) combined with yellow phosphors, which provides high efficiency up to more than 80%. One alternative way for generating white light consists of using red green blue (RGB) emission by coupling nitride (InGaN) and phosphide (AlInGaP) material systems for blue/green and red

colors, respectively. Despite lower efficiency, this phosphor-free solution gives rapid recombination lifetime allowing high speed operation required for specific applications, such as the emerging light fidelity (LiFi) technology.<sup>[1]</sup>

Alternative phosphor-free solutions have emerged in the literature for planar structures. For instance, dual-color LED devices have been reported by coupling either phosphide and nitride semiconductors by adhesive bonding to get red/green emission,<sup>[2]</sup> or also by growing monolithic dual-color blue/green and blue/yellow InGaN wells by molecular beam epitaxy (MBE)<sup>[3]</sup> or reversed nitride blue/green LED structures with the same p-GaN layer by metal-organic vapor phase epitaxy (MOVPE).<sup>[4]</sup> Systematic studies of such dual-color LED systems have been mainly performed by MOVPE to optimize color emission.<sup>[1,5–7]</sup> Improvements of efficiency performance have been reported at high currents using tunnel junction<sup>[8,9]</sup> and the green gap issue has been mitigated with the dual-color multiple quantum well (MQW) system in comparison with single-color MQWs.<sup>[10]</sup> The indium phase separation inside InGaN QWs has also been proposed to get a dual-color emission.<sup>[11,12]</sup> The multicolor emission is not limited to dual-color structure because monolithic nitride trebled-color RGB LED has even been also successfully demonstrated for white emission.<sup>[13]</sup>

Dr. A. Kapoor, V. Grenier, Dr. B. Gayral, Dr. C. Durand  
CEA, IRIG, PHELIQS, NPSC  
Univ. Grenoble Alpes  
Grenoble 38000, France  
E-mail: christophe.durand@cea.fr

Dr. E. Robin  
CEA, IRIG, MEM, LEMMA  
Univ. Grenoble Alpes  
Grenoble 38000, France

 The ORCID identification number(s) for the author(s) of this article can be found under <https://doi.org/10.1002/adpr.202000148>.

© 2021 The Authors. Advanced Photonics Research published by Wiley-VCH GmbH. This is an open access article under the terms of the Creative Commons Attribution License, which permits use, distribution and reproduction in any medium, provided the original work is properly cited.

Prof. C. Bougerol, Dr. G. Jacopin  
Grenoble INP\*, CNRS, Institut Néel  
Univ. Grenoble Alpes  
Grenoble 38000, France

Prof. M. Tchernycheva  
Centre de Nanosciences et de Nanotechnologies (C2N)  
CNRS UMR 9001  
University Paris-Saclay  
91120 Palaiseau, France

Dr. J. Eymery  
CEA, IRIG, MEM, NRS  
Univ. Grenoble Alpes  
Grenoble 38000, France

DOI: 10.1002/adpr.202000148

Apart from planar structures, the demonstration of LED devices with color mixing has been reported for different types of nanostructures. Using selective area growth (SAG), stripe growth leads to both polar and semipolar planes for InGaN QW growth,<sup>[14–16]</sup> and truncated hexagonal pyramid results in blue/green dual-color LED devices,<sup>[17]</sup> while multifaceting of microdonuts exhibits triple-color emission<sup>[18]</sup> that can be selectively excited by adjusting applied voltage.<sup>[19]</sup> In the case of nanowires, several demonstrations have also been reported mainly focused on axial heterostructures. Arrays of ordered nanowires obtained by top-down etching of monolithic dual-color planar structures show higher photoluminescence (PL) intensity as compared with the planar structure due to light extraction enhancement.<sup>[20,21]</sup> Multicolor EL emission (including RGB system) has been obtained by axial InGaN insertions along GaN nanowires grown by MBE.<sup>[22–25]</sup> Nanowire-based LEDs with blue core/shell InGaN/GaN MQWs combined with phosphors reach measured external quantum efficiency as high as 9% for white light emission.<sup>[26–28]</sup> Core-shell InGaN/GaN heterostructures can also exhibit multicolor emission related to different indium incorporation on specific crystallographic facets and edges.<sup>[29–31]</sup> For instance, Choi et al. reported orthogonally polarized dual-wavelength emission from InGaN/GaN core-shell microrod arrays due to different indium content in the *m*-plane facets compared with the edges leading to spatially separated blue and green emissions.<sup>[30]</sup> LEDs involving pencil-shape Ga-polar nanowires exhibit the same behavior as the truncated pyramids with the tuning of the emission from red to blue with the increase in voltage bias.<sup>[32]</sup> Although many groups have shown the color mixing due to empirical In-content variation with faceting,<sup>[29,30,32,33]</sup> the growth of core-shell wires with intentional indium variation in InGaN active layers remains an unexplored approach for multicolor emission. However, the core-shell geometry benefits of larger active region area and nonpolar surfaces promising for GHz-class LED devices.<sup>[34]</sup> In previous works, our group has separately reported blue and green emissions based on *m*-plane core-shell InGaN/GaN MQW grown on GaN wires,<sup>[35,36]</sup> and the current work targets phosphor-free dual-color emission by combining these two sets of MQW structures incorporating different In compositions.

Therefore, we performed the growth of two monolithic MQW sets in core-shell geometry around GaN microwires by MOVPE, composed of standard 3 × MQWs and In-rich 7 × MQWs. The dual blue-green emission has been demonstrated combining optical and structural characterization. Also, to highlight the interest of this epitaxial monolithic integration, the dual-color wires are integrated in a flexible LED demonstrator.

## 2. Results and Discussion

### 2.1. Sample Description

Self-assembled N-polar GaN wires (that may exhibit internal domain boundary inversions)<sup>[37,38]</sup> are grown without catalyst in a close coupled showerhead MOVPE reactor with the silane-assisted method described in the study by Koester et al.<sup>[39]</sup> Then, the core-shell heterostructure is grown starting by 3 × standard blue InGaN MQWs followed by 7 × In-rich green

InGaN MQWs using the same growth parameters reported in previous studies.<sup>[35,36]</sup> for blue and green emission, respectively (see all growth details in the Experimental Section). The first MQW set targeting lower indium content is positioned underneath the second MQW set with higher indium content to minimize the epitaxial strain at the beginning of the epitaxial stacking. A larger number of green MQWs compared with the blue have been basically chosen to compensate the expected lower efficiency of the green emission with respect to the blue.

**Figure 1a** shows the schematic of the dual-color core-shell InGaN/GaN heterostructure including the two MQW sets, named hereafter the first MQW set (standard blue 3 × MQWs) followed by the second MQW set (In-rich green 7 × MQWs). Note that the thicknesses of GaN barriers are different between the two MQW sets due to the change in growth temperatures and durations. The 30° tilted scanning electron microscopy (SEM) observation of as-grown wires on sapphire is shown in **Figure 1b** with an enlarged image focused on a typical single wire. The wire length is in the range of 35–40 μm for a wire diameter around 1.0–1.5 μm. The average wire density is estimated

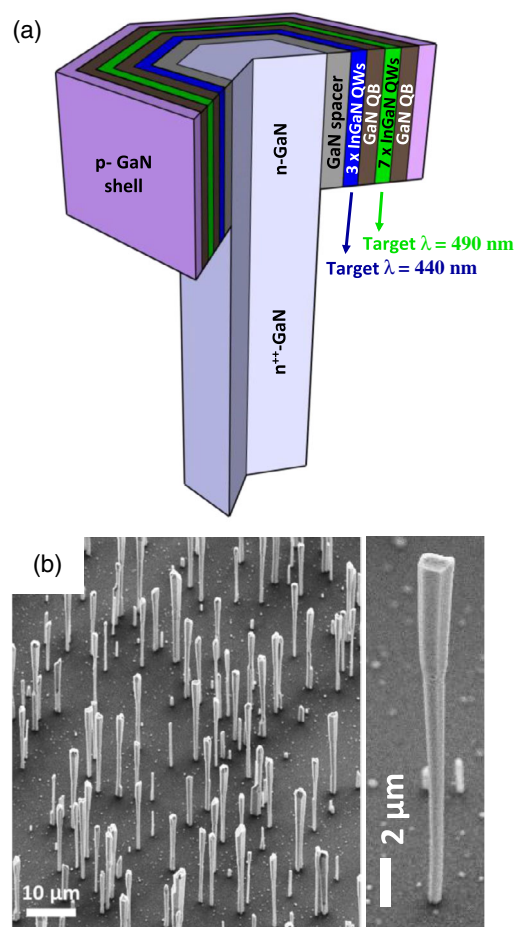


**Figure 1.** a) Schematics of the *m*-plane InGaN/GaN dual heterostructure containing the first 3 × InGaN MQW set and the second 7 × InGaN MQW set with targeted blue and green emission, respectively; b) 30° tilted SEM images of the wire ensemble showing core-shell geometry (left) and an enlarged image focused on single wire (right).

around  $10^6$  wire  $\text{cm}^{-2}$ . The core-shell growth occurs only on the wire upper part corresponding to n-GaN section grown without silane flux. A  $\text{SiN}_x$  layer is formed at the wire sidewalls of the  $\text{n}^+$ -GaN section resulting from silane injection and acts as a passivation layer to avoid any lateral growth.<sup>[40,41]</sup>

## 2.2. Optical Characterization

The optical properties of the as-grown wire ensembles are first investigated by PL measurements. **Figure 2** shows the temperature-dependent PL (TD-PL) spectra for a fixed laser power of  $100 \mu\text{W}$  and the power-dependent PL (PD-PL) spectra at 5 K. The peak at 360 nm, present in both PL measurements, corresponds to the GaN near band edge (NBE) and the two distinct contributions observed around 435 and 485 nm are fully consistent with the two different MQW sets targeting a blue and green emission, respectively. Multiple peak shoulders between 500 and 550 nm in the TD-PL spectra (see Figure 2a) are also observed mainly at low temperatures. These additional contributions arise from large indium fluctuations in In-rich regions inside QWs inducing a red-shifted emission,<sup>[36]</sup> as it will be confirmed later by cathodoluminescence (CL) measurements. Based on the ratio of the PL intensity between 300 and 5 K, the upper limit of the internal quantum efficiency (IQE) at a fixed laser power is estimated to be 33.5% and 18% for the emission at 435 and 485 nm, respectively. A lower IQE value for longer wavelength emission is generally observed due to strain-induced defects.<sup>[42]</sup> The IQE is also related to the localized states due to

local indium compositional fluctuations for high In-content QWs.<sup>[43]</sup> Furthermore, the PL intensity of the emission at 485 nm dominates the emission peak at 435 nm (almost doubled) at 5 K. This higher intensity can be associated with the larger number of QWs with In-rich composition. Also, as the excitation depth of PL laser is limited (about 200 nm for nitride materials at this wavelength), the PL intensity of the MQWs with higher In content closer to the surface is enhanced compared with the one of buried MQWs related to blue light emission. Moreover, the inner QWs emitting blue light can additionally contribute as an excitation source of green outer QWs. When the PL temperature increases, the nonradiative recombinations are enhanced for In-rich MQWs leading to lower IQE of In-rich MQWs as mentioned earlier, so that comparable PL intensities are observed for both contributions at room temperature. Furthermore, the temperature dependence of the peak position is analyzed for both contributions (see Figure 2b). A dependence following a well-known “S-shape” behavior is observed. Such behavior usually obtained in InGaN materials is attributed to carrier thermalization from localized to extended states as the temperature is increased.<sup>[44]</sup> The evolution of MQW peak energy at high temperature is compared with the Varshni’s equation:  $E(T) = E(T = 0 \text{ K}) - \alpha T^2 / (T + \beta)$ , where  $E(T)$  is the theoretical evolution of the transition energy as a function of temperature, and  $\alpha$  and  $\beta$  are two empirical constants ( $\alpha = 2.3 \text{ meV K}^{-1}$  and  $\beta = 1750 \text{ K}$ ).<sup>[45]</sup> An estimation of the mean localization energy  $E_{\text{loc}}$  can be deduced from the difference between experimental data and the Varshni’s equation at low temperature ( $T = 0 \text{ K}$ )

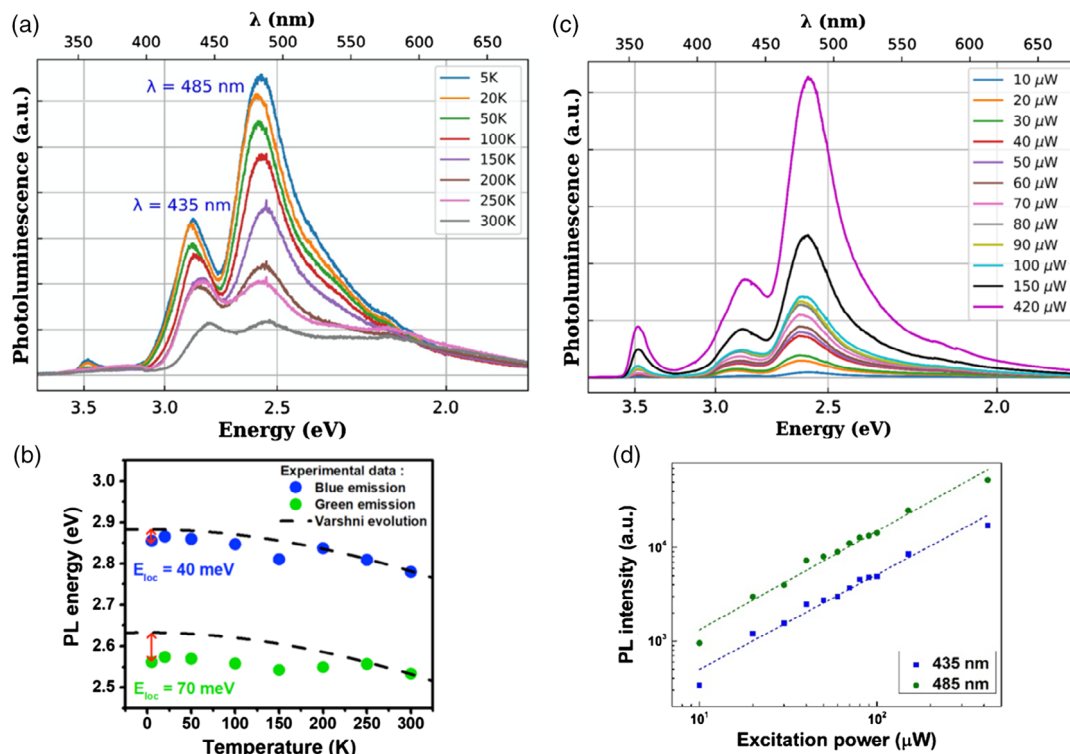


**Figure 2.** PL measurement performed on as-grown wires with a 244 nm laser: a) TD-PL spectra for a fixed laser power of  $100 \mu\text{W}$ ; b) the temperature dependence of the PL peak positions for the 435 and 485 nm contributions including the Varshni’s evolution; c) excitation PD-PL spectra for a fixed temperature at 5 K; d) the power dependence of PL intensities for the two contributions at 435 and 485 nm, respectively.

and is equal to 40 and 70 meV for blue and green QWs, respectively. This is consistent with the larger carrier localization energy for In-rich QWs.<sup>[46,47]</sup>

In addition, PD-PL measurements at 5 K in Figure 2c are performed for laser excitation powers ranging from 10 to 420  $\mu\text{W}$  ( $3\text{--}130\text{ W cm}^{-2}$ ). Under high power excitation (i.e., high carrier density regime), a screening of electric field typically occurs in polar *c*-plane QWs that induces a blue shift of the PL emission accompanied by a peak narrowing.<sup>[48]</sup> In the current study, the luminescence for both 435 and 485 nm contributions does not exhibit any significant shift with the excitation power increase. This agrees with the feature of nonpolar *m*-plane QWs emission, not affected by the *c*-axis polarization induced electric field. Moreover, we checked that the evolution of the PL intensity *I* as a function of the laser excitation power *P* obeys the relationship  $I \propto P^\alpha$  (see Figure 2d). The fitted  $\alpha$  values for both 435 and 485 nm contributions are close to unity: 1.01 ( $\pm 0.06$ ) and 1.05 ( $\pm 0.05$ ), therefore evidencing the predominance of radiative recombination at low temperature for both families of nonpolar QWs in the carrier density range we explored in this experiment.<sup>[49]</sup>

Afterward, the spatial localization of the emission of the two colors is studied by low-temperature CL experiments performed on dispersed wires on silicon substrates. Figure 3a shows the SEM image of a typical single wire. The corresponding CL mappings integrated over wavelength ranges related to both blue (430–440 and 450–460 nm) and green (480–490 and 490–500 nm) contributions are, respectively, shown in Figure 3b,c using the same intensity scale and the CL spectrum of the whole wire is shown in Figure 3d. Both 430–440 and 480–490 nm signals (previously observed in the PL measurements) are emitted from the core–shell active part located at the lateral upper part of wire. No specific *c*-plane or semipolar emission is detected at the wire top-flat surface. The 430–440 nm contribution is not uniformly distributed along the core–shell part because the higher intensity is mainly observed toward the wire top part (Figure 3b). On the contrary, a more uniform emission is observed for the CL maps near green region (480–500 nm) in Figure 3c. On the CL

spectrum (Figure 3d), the 435 nm emission at low temperature is more intense than the 485 nm one, contrary to PL results. This observation is probably explained by the difference in excitation depth: in nitrides, the nonresonant PL probes a typical depth of 200 nm considering the Lambert–Bert law for a laser excitation at 244 nm, whereas the CL probes around 300–400 nm with electron accelerated at 10 kV. Consequently, the PL favors the emission of QWs close to the surface (here, the QW emitting at 480–490 nm), whereas the CL excites more efficiently the deeper QWs emitting at 430–440 nm. CL spectra performed on several wires reveal a relatively stable wavelength emission (wire-to-wire variation within  $\pm 10\text{ nm}$ ) for both blue and green contributions. On the contrary, the ratio intensity can strongly change from one wire to another that makes difficult the direct comparison between PL and CL measurements performed on wire ensembles and on single wires, respectively. However, the CL measurements undoubtedly confirm that the dual-color emission comes from the nonpolar *m*-plane wire sidewalls.

### 2.3. Structural Characterization

For scanning transmission electron microscopy (STEM) structural characterization, a thin wire slice is prepared by focused ion beam (FIB) in longitudinal cross section along the *a*-zone axis. The STEM image at low magnification of the top part of the wire slice is shown in Figure 4a, where the InGaN QWs appear bright, while the GaN (wire core and barriers) appears dark. The presence of a flat surface as well as a pyramidal tip at the wire top is related to a dual polarity corresponding, respectively, to N-phase and Ga-phase separated by an inversion domain boundary (IDB).<sup>[37]</sup> The presence of minor Ga-phase polarity is commonly observed in such GaN wires grown on sapphire substrates prepared by a nitridation step.<sup>[50]</sup> Figures 4b,c shows two successive enlargements of the previous STEM image enabling a closer view of the *m*-plane radial InGaN QWs on the wire sidewall. The two families of InGaN/GaN MQWs are

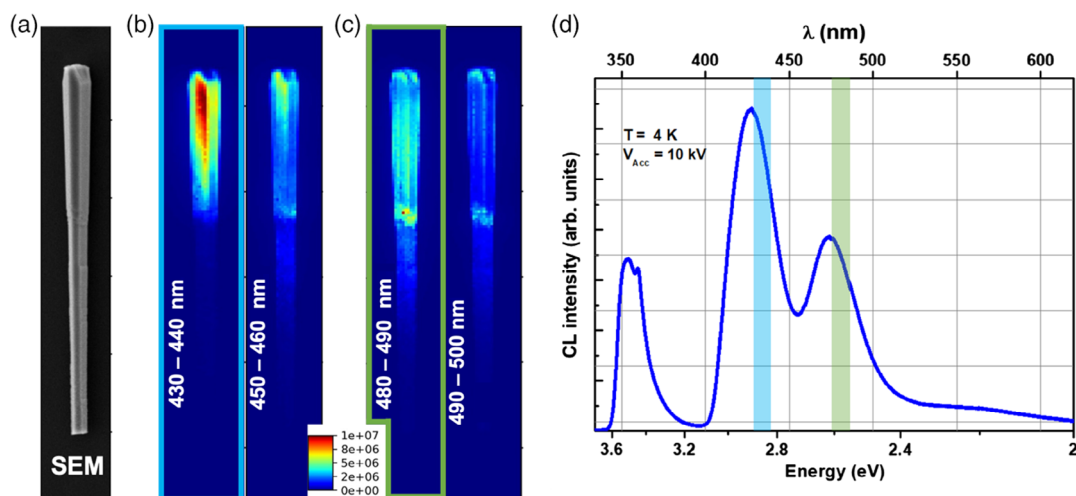


**Figure 3.** CL measurements at 4 K of a typical single wire. a) SEM image, b,c) CL mapping integrated near the blue range emission (430–440 and 450–460 nm) and near the green range emission ranges (480–490 and 490–500 nm), and d) CL spectrum integrated on the whole single wire.

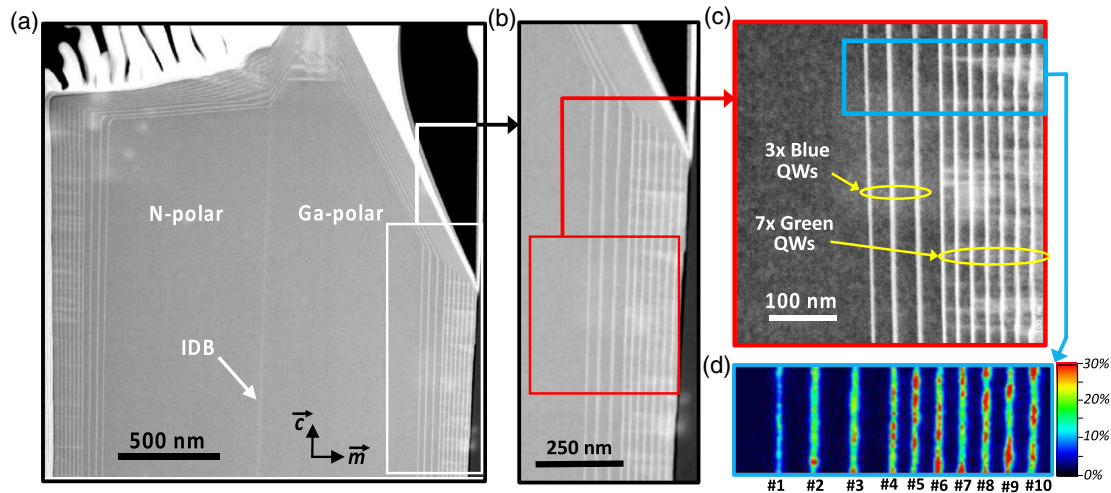


**Figure 4.** STEM-HAADF images of a longitudinal cross section of wire taken along the  $a$ -axis zone axis. a) Top part of the wire slice shows dual N- and Ga-polarity separated by an IDB with an enlarged view in (b) corresponding to the white square; c) STEM image corresponding to the red square in (b) showing the first  $3 \times$  MQW set with higher thickness and the second  $7 \times$  MQW set with lower thickness (as indicated by yellow arrows); d) EDX elemental mapping for the blue square in (c) representing the indium distribution in 10 InGaN QWs labeled as #1–#10.

noticeably observed: the first MQW set exhibiting three thicker barriers as compared with the following second MQW set. For the first set including blue  $3 \times$  MQWs, high-angle annular dark-field (HAADF) images do not reveal structural defects. The absence of defect is expected because the growth of a GaN spacer prior the QWs prevents the formation of any extended defect by burying the ultrathin SiGaN layer induced by residual silane in the reactor chamber.<sup>[51]</sup> On the contrary, we observe bright white lines originating perpendicularly to the first QW interface of the second set of green  $7 \times$  QWs and propagating to the free surface (see Figure 4a–c). These lines correspond to the formation of extended defects such as stacking faults, as previously reported for blue and green core-shell QWs.<sup>[35,36]</sup> The formation of these defects is attributed to the plastic strain relaxation due to expected higher indium composition present in the second MQW set that induces a larger lattice mismatch. The energy-dispersive X-ray (EDX) indium mapping, shown in Figure 4d, corresponding to the blue square region, marked in Figure 4c, demonstrates that the In content in the second MQW set is increased with respect to the first MQW set. In addition, the presence of In-rich clusters (red zones) inside QWs is largely increased for the second MQW set.

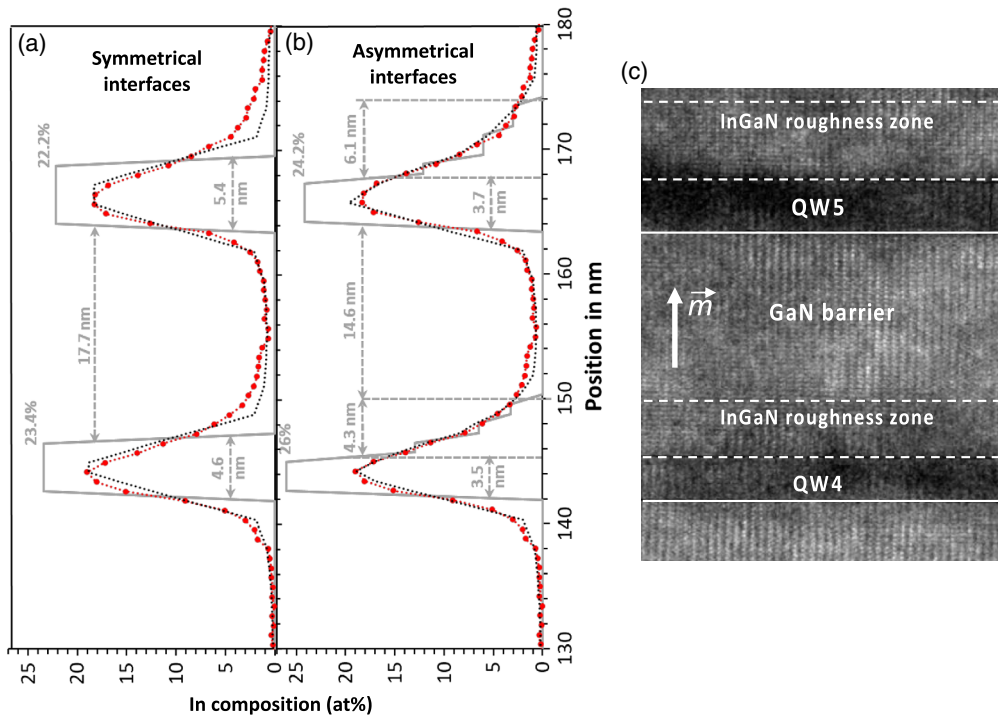
To confirm this observation, another area of the slice has been analyzed by EDX with a higher resolution to extract the indium composition inside the two sets of QWs. These detailed analyses of EDX measurements of core-shell InGaN MQWs are shown in Figure 5 and 6.

Figure 5 shows the best fit providing the effective In profile along the  $m$ -axis for two QWs (QW #4 and #5) combined with a high-resolution TEM image corresponding to the same QWs. In Figure 5a,b, the measured In profile corresponds to the red dotted line, which has to be corrected by considering the beam broadening induced by electron scattering processes to get the effective In profile along the core-shell structure. This correction is performed by assuming a Gaussian distribution of the beam broadening with a minimum beam diameter at the top

illuminated surface of 0.2 nm and a maximum beam diameter at the base of the sample computed using the universal equation of Gauvin and Rudinsky<sup>[52]</sup> considering the beam convergence angle, the local composition and mass thickness of the sample determined from the zeta-factor method (typically 10 nm for a 100 nm-thick sample).

Two different models of the actual In profile have been used to fit the measured In profile of InGaN QWs corresponding to 1) symmetrical sharp interfaces and 2) asymmetrical interfaces (sharp barrier/QW lower interface vs graded QW/barrier upper interface), as depicted using a gray solid line in Figure 5a,b, respectively. For the sake of simplicity, the graded QW/barrier upper interface is modeled by three successive layers of constant thickness for which the In content decreases by a factor of 2 from one layer to another (the first layer containing half the In content of QW, the second the quarter, and the last the one-eighth). Figure 5a shows that the dashed line fit using the symmetric model is not optimal for the upper QW/barrier interfaces. On the opposite, the asymmetrical model in Figure 5b correctly fits both interfaces. The model type significantly changes the value of QW thickness. However, the variation of In content inside QW is much less affected because a difference of only 3% of In content is found. We note that the upper QW/barrier interface is relatively thick: more than 4 and 6 nm for the QW#4 and #5, respectively. This interface corresponds to a zone with detectable EDX In content ( $[In]/[Ga] > 1\%$ ) related to the large roughness of InGaN growth on GaN.<sup>[53]</sup> This intermediate zone is called “InGaN roughness zone” in Figure 5c. The asymmetrical model is thus consistent with the TEM observation exhibiting also rough upper InGaN/GaN interface, contrary to the first sharp GaN/InGaN interface. In the following, the model based on asymmetrical interface will be used to determine the In composition for the core-shell QWs.

Figure 6 shows the in-plane and out-of-plane In composition from EDX measurements for the two MQW sets. Figure 6a shows the In mapping of all QWs with a scale bar ranging from



**Figure 5.** Fit optimization of the In profile from EDX measurements performed on the QW#4 and #5 along the  $m$ -axis combined with the corresponding high-resolution TEM image. a) Fit with symmetrical interface model; b) fit with asymmetrical interface model with the EDX measured In profile shown in red dotted line, the effective In profile model in grey line and the fit of experimental data using the selected model in black dotted line; c) high-resolution TEM image of QW#4 and QW#5 showing the InGaN roughness zone above the QW/barrier interfaces.

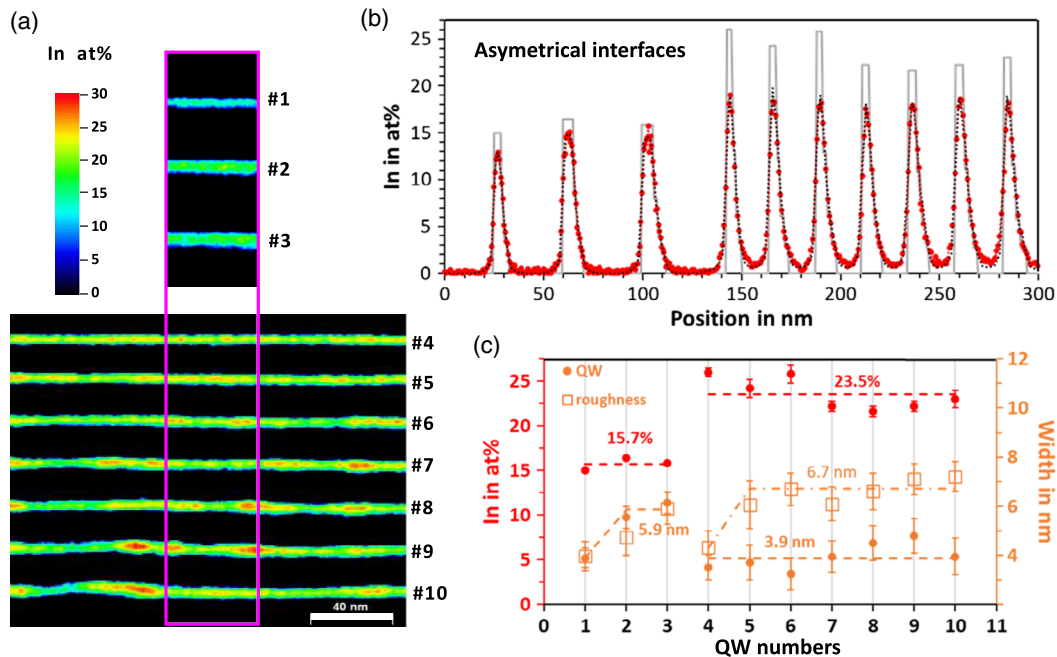


**Figure 6.** In-plane and out-of-plane indium composition from EDX measurements of the core-shell heterostructure including two MQW sets. a) Indium EDX elemental mapping for 3 × QWs and 7 × QWs with a color scale showing In composition in atomic percentage; b) In profiles along  $m$ -axis as a function from the innermost to the outermost QW including the measured In-content profile (red dots), an effective In-content profile based on the asymmetrical interfaces model (gray line) and the corresponding fit (black dotted line); c) evolution of In content and the thicknesses of QWs and “InGaN roughness zone” for the first 3 × MQW set (#1–#3) and the second 7 × MQW set (#4–#10), determined by the asymmetrical interface model to fit EDX data as shown in (b).

0% to 30%. As already observed in Figure 4c, the indium distribution is relatively homogeneous in the first MQW set, while significant indium fluctuations are observed for the second MQW set. The larger area of the second QW set exhibits many In-rich zones (red color). This large indium variation can be related to demixing effect of In-rich InGaN, and also to the presence of extended defects that can locally favor the In-composition variation because such defects are only observed for the second MQW set. Such assumption is suggested by the increase in In composition close to stacking faults already measured by atom probe tomography on a similar type of core-shell InGaN MQWs.<sup>[54,55]</sup>

The In content profile is then extracted by integrating over a 40 nm-wide rectangle (pink line marked in Figure 6a) and is shown in Figure 6b. Based on the aforementioned fit procedure (see Figure 5), the measured In profile (red dots) is correctly fitted (black dotted line) considering asymmetrical interface model for the effective In profile (gray line). It allows determining the In content and thicknesses of the QWs and also the thickness of the InGaN roughness zone, which are plotted in Figure 6c for all the QWs.

The first MQW set exhibits an average QW thickness of about 5.9 ( $\pm 0.5$ ) nm, whereas a thinner average QW thickness equal to 3.9 ( $\pm 0.7$ ) nm is measured for the second  $7 \times$  QW set. The first well of each QW family is not included in the average QW thickness value because it has a lower thickness compared with the successive wells, as also observed in the STEM-HAADF images in Figure 4 (the deviation is attributed to a transition in growth temperature occurring for the first growth cycle of the QW family). The thickness of InGaN roughness zone is significant (in the range of 5–7 nm) with slightly higher value ( $+0.8$  nm) for green QWs. The first QW of each MQW set leads to a thickness reduction of the InGaN roughness zone, which is again attributed to nonstabilized growth parameters during the first cycle. The corrected EDX measurements reveal a higher In composition estimated to be about 23.5 ( $\pm 2$ )% for the second MQW set compared with 15.7 ( $\pm 0.5$ )% for the first MQW set. These values are consistent with the emission wavelengths measured by PL and CL measurements. Moreover, the QW-to-QW distribution of average In content is quite low (less than 4%), whereas a large variation of the In content (from 15% to 30%) is observed inside individual green QW with In-rich clusters exhibiting In content up to 30%. These local composition fluctuations are consistent with localization effects previously

observed in luminescence analyses and may explain the long-wavelength PL emission tail corresponding to green–yellow range (500–600 nm) of the PL emission peak (see Figure 2). Also, the presence of extended defects only observed for the second MQW set can be attributed to the QW thickness that exceeds the critical thickness of InGaN layer grown on *m*-plane GaN estimated to about 3 nm for an In content equal of 23–24% considering nonbasal plane dislocations.<sup>[56]</sup> Based on thickness and In content determined by EDX, the emission energy at 300 K of *m*-plane InGaN QWs is calculated with 8-band *k*-*p* model of about 430 and 470 nm for blue and green contributions.<sup>[57]</sup> The red-shifted discrepancy of about 20 nm observed in the PL experimental data (Figure 2a) can be attributed to localization effects and the presence of stacking faults.<sup>[54]</sup>

## 2.4. Integration in a Flexible LED Device

After these thorough structural and optical characterizations, these wires with an additional 70 nm-thick p-doped GaN shell have been used to fabricate a dual-color emission flexible LED device. The fabrication process described in previous reports<sup>[28,58,59]</sup> is based on the embedding of wires in a polydimethylsiloxane (PDMS) polymer layer, which is then peeled-off and transferred on a host flexible surface after making electrical contacts. Figure 7a shows a picture of the green EL emission performed at room temperature obtained for a bias voltage of 8 V of a large flexible LED (4 cm<sup>2</sup>) with embedded dual-color wires. EL spectra are recorded by collecting the light by an optical fiber at the top of the sample. EL spectra, shown in Figure 7b in logarithmic scale, exhibit a broad EL peak (460–560 nm) centered at 500 nm, leading to green emission whatever the applied bias voltage in the range of 7–9.5 V. Only the second green MQW set contributes to the EL emission. The broadening of EL peak is attributed to the large In fluctuations inside the QWs previously revealed by EDX analyses. The absence of EL emission from the first blue MQW set is related to the low hole mobility. As the hole concentration significantly decreases inside QWs as we move away from the p-GaN shell, holes are almost not injected in the buried blue MQWs. It thus explains the predominance of green emission observed in the EL of Figure 7a,b. Similarly, this behavior has been observed for planar dual-color heterostructures, where the EL of  $3 \times$  blue QWs followed by  $2 \times$  green

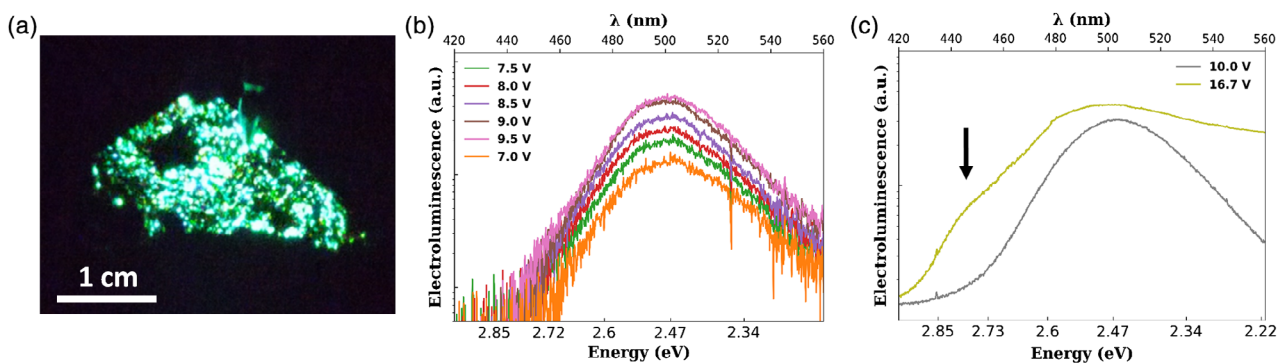


**Figure 7.** Electrical measurements of the dual-color LED at 300 K: a) photograph of the LED under operation showing green color emission (8 V); b) typical EL spectra when the applied bias changes from 7.0 to 9.5 V; and c) EL spectra at another position for applied bias voltage at 10 and 16.7 V.

QWs exhibits only green emission at different forward currents.<sup>[6]</sup> The bias voltage has been further increased for the flexible LED. At only one position corresponding certainly to local higher current injection, the EL emission presented in Figure 7c shows a weak blue contribution at 450 nm for a bias voltage as high as 16.7 V, whereas the typical green peak is measured at 10 V. In this case, the dual emission is observed with EL excitation. However, a longer wavelength parasitic emission (beyond 560 nm) also appears at such a high voltage. It can be tentatively explained by a current overshoot. Indeed, as no electron blocking layer is inserted in the MQW core/shell heterostructures, an overshoot of the electron flow over the MQW structure may occur resulting in an activation of deep defects in the p-GaN shell emitting in the long wavelength range. It should be noted that in the current study, the core-shell dual-emission MQW heterostructure is optimized for PL and CL measurements; however, it requires changes for an efficient dual-color EL emission. Bandgap engineering has been reported for planar structures to favor the hole injection into the whole MQW heterostructures by adding a GaN spacer in InGaN/InGaN MQWs<sup>[1]</sup> or AlGaN interlayers acting as intermediate carrier blocking layers in InGaN/GaN MQWs.<sup>[13]</sup> An improvement in the MQW heterostructure design for EL emission can also be performed by reducing the total number of QWs to facilitate efficient transport of charge carriers across the whole active region. Also, the growth of inverted dual-color structure with inner green QWs and outer blue QWs is also an interesting approach to limit reabsorption and favor the hole injection.<sup>[1]</sup> Recently, an improved hole injection between two core-shell InGaN QW systems has also successfully been reported by the use of a tunnel junction.<sup>[60]</sup> This strategy may be potentially applied to the core/shell wire LEDs.

### 3. Conclusion

In conclusion, dual-color emission is reported from GaN wires containing two monolithic core-shell MQW sets (blue  $3 \times$  MQWs and green  $7 \times$  MQWs) correlating structural, optical, and electro-optical characterizations. PL measurements reveal two different wavelength emissions in the ranges of 400–450 and 450–550 nm, respectively. Additional CL mappings confirm that both emissions originate from the two MQW sets grown on nonpolar *m*-plane wire sidewalls. Based on a quantitative EDX analysis with asymmetrical QW/barrier interfaces, the In content has been measured to be 15.7 ( $\pm 0.5$ )% and 23.5 ( $\pm 2$ )% for the first and the second MQW set, which is coherent with the observed dual blue-green emission. The fabrication of a flexible LED device using these dual-color wires has also been performed. EL is dominated by the green emission due to the poor hole mobility that limits the carrier injection in blue QWs located away from the p-GaN shell. This work demonstrates the possibility of color mixing based on core-shell MQW geometry for nanowire-based applications.

### 4. Experimental Section

**MOVPE Growth of Core-Shell Microwires:** GaN wires were grown on nitridated *c*-plane sapphire substrates at 1040 °C with V/III ratio equal to 50 using a silane flow of 200 nmol min<sup>-1</sup> to strongly limit the lateral

growth during 300 s.<sup>[39]</sup> The GaN wire stem was heavily n<sup>++</sup>-doped ( $N_d \approx 10^{20}$  cm<sup>-3</sup>) by the initial high silane flow.<sup>[39,61]</sup> The silane flux was then switched off for 400 s. The wires continued to grow due to the remaining silane present inside the reactor leading to an additional wire length of about 15 μm with a residual n-type doping level ( $N_d \approx 10^{18}$  cm<sup>-3</sup>).<sup>[62]</sup> A GaN spacer was then radially grown around the wire core at 900 °C for 100 s under N<sub>2</sub> to prevent the degradation of InGaN QWs from residual Si contamination present at the wire sidewalls.<sup>[51]</sup> This step was followed by the radial growth of  $3 \times$  InGaN MQWs at 720 °C for 75 s separated by GaN barriers grown at 900 °C for 150 s to target low indium content ( $\approx 15\%$ ), as described in the study by Koester et al.<sup>[35]</sup> The growth of a third GaN barrier was then followed by the growth of  $7 \times$  InGaN MQWs at 680 °C for 40 s separated by GaN barriers grown at 885 °C for 80 s to target higher indium content ( $\approx 20\%$ ), according to the growth conditions reported in the study by Kapoor et al.<sup>[36]</sup> The choice to first grow  $3 \times$  QWs at higher temperature prevented any degradation of In-rich  $7 \times$  QWs grown at a lower temperature. For the fabrication of wire-LED devices, a 70 nm-thick p-doped GaN shell was additionally deposited at 920 °C during 420 s followed by a dopant activation annealing at 700 °C during 20 min.

**PL Measurements:** A continuous wave frequency doubled solid-state laser at 244 nm was used to excite the wire ensembles with a spot size of about 50 μm. The excitation was performed with an angle of about 45° allowing to excite simultaneously the wire sidewall and the wire top due to low wire density. The signals were collected from the top side of samples with a 600 grooves cm<sup>-1</sup> grating spectrometer equipped with a liquid nitrogen cooled charge coupled device camera.

**CL Measurements:** The wires were excited with an electron beam having an acceleration voltage of 10 kV and a probe current of about 1 nA. A parabolic mirror was used to collect the CL signal, which was analyzed by a grating monochromator and a Peltier cooled CCD camera.

**STEM Observation and EDX Quantitative Analysis:** The STEM images were acquired at 200 kV with the HAADF detector using either a FEI Thermo Fischer Tecnaï or a FEI Themis microscope. The EDX acquisition was performed at a beam current of 400 pA with a beam convergence angle of 20 mrad and a pixel size of 0.2 nm (comparable with the probe diameter at the sample surface). X-ray spectra were extracted by summing all pixels over the *c*-axis along the *m*-axis, followed by their deconvolution and background subtraction using the QUANTAX-800 software. This operation allowed extracting the net intensity of X-ray lines generated by the elements present along the beam axis, i.e., K- and L-lines of Ga, L-lines of In, and K-lines of N. The conversion of net X-ray intensity into atomic concentration was performed using the zeta-factor method allowing a simultaneous determination of concentrations and mass thicknesses. This method used the zeta-factor for Ga K- and L-lines, In L-lines, and N K-lines measured on reference samples with known composition and mass thicknesses under the same operating conditions in the same equipment.<sup>[63,64]</sup>

**Flexible LED Fabrication:** After the spin-coating of PDMS on as-grown wires, this hybrid layer was mechanically peeled-off before mounting it on a host conductive and flexible support (copper tape in the present demonstrator). Reactive ion etching was performed to etch partially the polymer layer to get 1–2 μm long wire segment protruding out of the PDMS. To obtain ohmic contacts, Ni/Au thin metallic bilayers were subsequently deposited only at the p-type GaN top part, while a composite metal layer Ti/Al/Ti/Au was added on the n-GaN side at the wire foots. To facilitate uniform current spreading and to insure a good flexible p-type contact, additional dense Ag-nanowire network was spin-coated onto the top PDMS layer (two Ag nanowire length was used: 40 and 120 μm). An annealing at 200 °C for 20 min under air was then performed to decompose the chemical solvents and promote the fusion of silver nanowires increasing the network conductivity.

### Acknowledgements

This work was financially supported by French National Labex GaNeX (ANR-11-LABX-0014) and by the EU ERC project “NanoHarvest” (grant

no. 639052). The authors would like to thank J. Dussaud for his work on the MOVPE setup and N. Mollard for his support in FIB preparation.

## Conflict of Interest

The authors declare no conflict of interest.

## Data Availability Statement

Research data are not shared.

## Keywords

dual-color emission, InGaN, light-emitting devices, nanowires, quantum wells

Received: November 17, 2020

Revised: January 20, 2021

Published online:

- [1] N. Poyiatzis, M. Athanasiou, J. Bai, Y. Gong, T. Wang, *Sci. Rep.* **2019**, 9, 1383.
- [2] C. M. Kang, S. J. Kang, S. H. Mun, S. Y. Choi, J. H. Min, S. Kim, J. P. Shim, D. S. Lee, *Sci. Rep.* **2017**, 7, 10333.
- [3] B. Damilano, N. Grandjean, C. Pernot, J. Massies, *Jpn. J. Appl. Phys.* **2001**, 40, L918.
- [4] D.-J. Kong, C.-M. Kang, J.-Y. Lee, J. Kim, D.-S. Lee, *Opt. Express* **2016**, 24, A667.
- [5] S. C. Shei, J. K. Sheu, C. M. Tsai, W. C. Lai, M. L. Lee, C. H. Kuo, *Jpn. J. Appl. Phys.* **2006**, 45, 2463.
- [6] Y. D. Qi, H. Liang, W. Tang, Z. D. Lu, K. M. Lau, *J. Cryst. Growth* **2004**, 272, 333.
- [7] Y. Meng, L. Wang, F. Li, G. Zhao, W. Yao, S. Yang, Z. Wang, *Mater. Res. Express* **2019**, 6, 0850c8.
- [8] M. Saha, A. Biswas, H. Karan, *Opt. Mater. (Amst.)* **2018**, 77, 104.
- [9] Z. C. Feng, L. H. Zhu, T. W. Kuo, C. Y. Wu, H. L. Tsai, B. L. Liu, J. R. Yang, *Thin Solid Films* **2013**, 529, 269.
- [10] Y. Jiang, Y. Li, Y. Li, Z. Deng, T. Lu, Z. Ma, P. Zuo, L. Dai, L. Wang, H. Jia, W. Wang, J. Zhou, W. Liu, H. Chen, *Sci. Rep.* **2015**, 5, 10883.
- [11] Z. L. Fang, Q. F. Li, X. Y. Shen, H. Xiong, J. F. Cai, J. Y. Kang, W. Z. Shen, *J. Appl. Phys.* **2014**, 115, 043514.
- [12] Q. Wang, X. Gao, Y. Xu, J. Leng, *J. Alloys Compd.* **2017**, 726, 460.
- [13] H. S. El-Ghoroury, M. Yeh, J. C. Chen, X. Li, C. L. Chuang, *AIP Adv.* **2016**, 6, 075316.
- [14] M. Funato, K. Hayashi, M. Ueda, Y. Kawakami, Y. Narukawa, T. Mukai, *Appl. Phys. Lett.* **2008**, 93, 021126.
- [15] W. Song, H. Chen, X. Luo, Y. Sun, X. Wang, H. Wang, D. Guo, M. Qi, G. Li, S. Li, *J. Alloys Compd.* **2019**, 791, 1241.
- [16] Y. Li, Y. Tong, G. Yang, C. Yao, R. Sun, L. Cai, G. Xu, J. Wang, Q. Zhang, X. Ye, M. Wu, Z. Wen, *J. Vac. Sci. Technol. A* **2015**, 33, 05E102.
- [17] M.-L. Lee, Y.-H. Yeh, S.-J. Tu, P. C. Chen, M.-J. Wu, W.-C. Lai, J.-K. Sheu, *Opt. Express* **2013**, 21, A864.
- [18] Y. H. Ko, J. Song, B. Leung, J. Han, Y. H. Cho, *Sci. Rep.* **2014**, 4, 5514.
- [19] Y. Tchoe, J. Jo, M. Kim, J. Heo, G. Yoo, C. Sone, G. C. Yi, *Adv. Mater.* **2014**, 26, 3019.
- [20] J. Zhao, X. Wei, D. Liang, Q. Hu, J. Yan, J. Wang, T. Wei, *J. Electron. Packag.* **2020**, 142, 031104.
- [21] L. Sen Feng, Z. Liu, N. Zhang, B. Xue, J. X. Wang, J. M. Li, *Chinese Phys. Lett.* **2019**, 36, 027802.
- [22] H. W. Lin, Y. J. Lu, H. Y. Chen, H. M. Lee, S. Gwo, *Appl. Phys. Lett.* **2010**, 97, 073101.
- [23] R. Wang, H. P. T. Nguyen, A. T. Connie, J. Lee, I. Shih, Z. Mi, *Opt. Express* **2014**, 22, A1768.
- [24] Y. Kamali, B. R. Walsh, J. Mooney, H. Nguyen, C. Brosseau, R. Leonelli, Z. Mi, P. Kambhampati, *J. Appl. Phys.* **2013**, 114, 164305.
- [25] Y. L. Chang, J. L. Wang, F. Li, Z. Mi, *Appl. Phys. Lett.* **2010**, 96, 013106.
- [26] T. Schimpke, M. Mandl, I. Stoll, B. Pohl-Klein, D. Bichler, F. Zwaschka, J. Strube-Knyrim, B. Huckenbeck, B. Max, M. Müller, P. Veit, F. Bertram, J. Christen, J. Hartmann, A. Waag, H.-J. Lugauer, M. Strassburg, *Phys. Status Solidi* **2016**, 213, 1577.
- [27] N. Guan, N. Amador-Mendez, J. Wang, S. Das, A. Kapoor, F. H. Julien, N. Gogneau, M. Foldyna, S. Som, J. Eymery, C. Durand, M. Tchernycheva, *J. Phys. Photonics* **2019**, 1, 035003.
- [28] N. Guan, X. Dai, A. Messanvi, H. Zhang, J. Yan, E. Gautier, C. Bougerol, F. H. Julien, C. Durand, J. Eymery, M. Tchernycheva, *ACS Photonics* **2016**, 3, 597.
- [29] G. Schmidt, M. Müller, P. Veit, S. Metzner, F. Bertram, J. Hartmann, H. Zhou, H. H. Wehmann, A. Waag, J. Christen, *Sci. Rep.* **2018**, 8, 16026.
- [30] S. Choi, H. G. Song, S. Cho, Y. H. Cho, *Nano Lett.* **2019**, 19, 8454.
- [31] G. Jacopin, D. L. A. Bugallo, P. Lavenus, L. Rigutti, F. H. Julien, L. F. Zagonel, M. Kociak, C. Durand, D. Salomon, X. J. Chen, J. Eymey, M. Tchernycheva, *Appl. Phys. Express* **2012**, 5, 014101.
- [32] Y. J. Hong, C.-H. Lee, A. Yoon, M. Kim, H.-K. Seong, H. J. Chung, C. Sone, Y. J. Park, G.-C. Yi, *Adv. Mater.* **2011**, 23, 3284.
- [33] C.-G. Tu, Y.-F. Yao, C.-H. Liao, C.-Y. Su, C. Hsieh, C.-M. Weng, C.-H. Lin, H.-T. Chen, Y.-W. Kiang, C. C. Yang, *Opt. Express* **2015**, 23, 21919.
- [34] M. Nami, A. Rashidi, M. Monavarian, S. Mishkat-UI-Masabih, A. K. Rishinaramangalam, S. R. J. Brueck, D. Feezell, *ACS Photonics* **2019**, 6, 1618.
- [35] R. Koester, J. Hwang, D. Salomon, X. Chen, C. Bougerol, J. Barnes, D. Le, S. Dang, L. Rigutti, A. D. L. Bugallo, G. Jacopin, M. Tchernycheva, C. Durand, J. Eymery, *Nano Lett.* **2011**, 11, 4839.
- [36] A. Kapoor, N. Guan, M. Vallo, A. Messanvi, L. Mancini, E. Gautier, C. Bougerol, B. Gayral, F. H. Julien, F. Vurpillot, L. Rigutti, M. Tchernycheva, J. Eymery, C. Durand, *ACS Photonics* **2018**, 5, 4330.
- [37] X. J. Chen, G. Perillat-Merceroz, D. Sam-Giao, C. Durand, J. Eymery, *Appl. Phys. Lett.* **2010**, 97, 151909.
- [38] S. Labat, M. I. Richard, M. Dupraz, M. Gailhanou, G. Beutier, M. Verdier, F. Mastropietro, T. W. Cornelius, T. U. Schüllli, J. Eymery, O. Thomas, *ACS Nano* **2015**, 9, 9210.
- [39] R. Koester, J. S. Hwang, C. Durand, D. L. S. Dang, J. Eymery, *Nanotechnology* **2010**, 21, 015602.
- [40] J. Eymery, D. Salomon, X. Chen, C. Durand, US 2014/0080290 A1, **2012**.
- [41] C. Tessarek, M. Heilmann, E. Butzen, A. Haab, H. Hardtdegen, C. Dieker, E. Spiecker, S. Christiansen, *Cryst. Growth Des.* **2014**, 14, 1486.
- [42] T. Langer, H. Jönen, A. Kruse, H. Bremers, U. Rossow, A. Hangleiter, *Appl. Phys. Lett.* **2013**, 103, 022108.
- [43] Y. Yang, X. A. Cao, C. Yan, *IEEE Trans. Electron Devices* **2008**, 55, 1771.
- [44] Y.-H. Cho, G. H. Gainer, A. J. Fischer, J. J. Song, S. Keller, U. K. Mishra, S. P. DenBaars, *Appl. Phys. Lett.* **1998**, 73, 1370.
- [45] H. Song, J. S. Kim, E. K. Kim, Y. G. Seo, S. M. Hwang, *Nanotechnology* **2010**, 21, 134026.
- [46] Q. Mu, M. Xu, X. Wang, Q. Wang, Y. Lv, Z. Feng, X. Xu, Z. Ji, *Phys. E* **2016**, 76, 1.
- [47] W. Liu, D. G. Zhao, D. S. Jiang, P. Chen, Z. S. Liu, J. J. Zhu, M. Shi, D. M. Zhao, X. Li, J. P. Liu, S. M. Zhang, H. Wang, H. Yang, *J. Alloys Compd.* **2015**, 625, 266.
- [48] T. Wang, D. Nakagawa, J. Wang, T. Sugahara, S. Sakai, *Appl. Phys. Lett.* **1998**, 73, 3571.

- [49] Q. Wang, Z. Ji, S. Qu, G. Wang, Y. Jiang, B. Liu, X. Xu, H. Mino, *Opt. Express* **2012**, *20*, 3932.
- [50] S. Labat, M.-I. Richard, M. Dupraz, M. Gailhanou, G. Beutier, M. Verdier, F. Mastropietro, T. W. Cornelius, T. U. Schüllli, J. Eymery, O. Thomas, *ACS Nano* **2015**, *9*, 9210.
- [51] A. Kapoor, S. Finot, V. Grenier, E. Robin, C. Bougerol, J. Bleuse, G. Jacopin, J. Eymery, C. Durand, *ACS Appl. Mater. Interfaces* **2020**, *12*, 19092.
- [52] R. Gauvin, S. Rudinsky, *Ultramicroscopy* **2016**, *167*, 21.
- [53] D. M. Graham, A. Soltani-Vala, P. Dawson, M. J. Godfrey, T. M. Smeeton, J. S. Barnard, M. J. Kappers, C. J. Humphreys, E. J. Thrush, *J. Appl. Phys.* **2005**, *97*, 103508.
- [54] L. Mancini, W. Lefebvre, J. Houard, I. Blum, F. Vurpillot, J. Eymery, C. Durand, L. Rigutti, *Appl. Phys. Lett.* **2016**, *108*, 042102.
- [55] L. Rigutti, I. Blum, D. Shinde, D. Hernández-Maldonado, W. Lefebvre, J. Houard, F. Vurpillot, A. Vella, M. Tchernycheva, C. Durand, J. Eymery, B. Deconihout, *Nano Lett.* **2014**, *14*, 107.
- [56] P. S. Hsu, M. T. Hardy, E. C. Young, A. E. Romanov, S. P. Denbaars, S. Nakamura, J. S. Speck, *Appl. Phys. Lett.* **2012**, *100*, 171917.
- [57] D. Salomon, *Croissance, Propriétés Optiques et Intégration d'hétérostructures Radiales InGaN/GaN Autour de Fils Auto-Assemblés de GaN Crûs Sur Saphir et Silicium*, **2013**.
- [58] X. Dai, A. Messanvi, H. Zhang, C. Durand, J. Eymery, C. Bougerol, F. H. Julien, M. Tchernycheva, *Nano Lett.* **2015**, *15*, 6958.
- [59] H. Zhang, X. Dai, N. Guan, A. Messanvi, V. Neplokh, V. Piazza, M. Vallo, C. Bougerol, F. H. Julien, A. Babichev, N. Cavassilas, M. Bescond, F. Michellini, M. Foldyna, E. Gautier, C. Durand, J. Eymery, M. Tchernycheva, *ACS Appl. Mater. Interfaces* **2016**, *8*, 26198.
- [60] Y.-H. Ra, C.-R. Lee, *Nano Lett.* **2020**, *20*, 4162.
- [61] P. Tchoufian, F. Donatini, F. Levy, B. Amstatt, P. Ferret, J. Pernot, *Appl. Phys. Lett.* **2013**, *102*, 122116.
- [62] P. Tchoufian, F. Donatini, F. Levy, A. Dussaigne, P. Ferret, J. Pernot, *Nano Lett.* **2014**, *14*, 3491.
- [63] M. Watanabe, D. B. Williams, *J. Microsc.* **2006**, *221*, 89.
- [64] M. Lopez-Haro, P. Bayle-guillemaud, N. Mollard, F. Saint-Antonin, C. Vilsteren, B. Freitag, E. Robin, in *18th Int. Microscopy Congress*, **2014**, p. 2428.